

Effect of temperature and mass transport on transition metal isotope fractionation during electroplating

Jay R. Black^{a,*}, Seth John^b, Edward D. Young^{a,c}, Abby Kavner^{a,c}

^a *Institute for Geophysics and Planetary Physics, University of California, Los Angeles, CA 90095, USA*

^b *Division of Geological and Planetary Sciences, California Institute of Technology, Pasadena, CA 91125, USA*

^c *Earth and Space Sciences, University of California, Los Angeles, CA 90095, USA*

Received 14 July 2009; accepted in revised form 4 May 2010; available online 23 July 2010

Abstract

Transition metal stable isotope signatures can be useful for tracing both natural and anthropogenic signals in the environment, but only if the mechanisms responsible for fractionation are understood. To investigate isotope fractionations due to electrochemistry (or redox processes), we examine the stable isotope behavior of iron and zinc during the reduction reaction $M_{\text{aqueous}}^{2+} + 2e^- = M_{\text{metal}}$ as a function of electrochemical driving force, temperature, and time. In all cases light isotopes are preferentially electroplated, following a mass-dependent law. Generally, the extent of fractionation is larger for higher temperatures and lower driving forces, and is roughly insensitive to amount of charge delivered. The maximum fractionations are $\delta^{56/54}\text{Fe} = -4.0\text{‰}$ and $\delta^{66/64}\text{Zn} = -5.5\text{‰}$, larger than observed fractionations in the natural environment and larger than those predicted due to changes in speciation. All the observed fractionation trends are interpreted in terms of three distinct processes that occur during an electrochemical reaction: mass transport to the electrode, chemical speciation changes adjacent to the electrode, and electron transfer at the electrode. We show that a large isotope effect adjacent the electrode surface arises from the charge-transfer kinetics, but this effect is attenuated in cases where diffusion of ions to the electrode surface becomes the rate-limiting step. Thus while a general increase in fractionation is observed with increasing temperature, this appears to be a result of thermally enhanced mass transport to the reacting interface rather than an isotope effect associated with the charge-transfer kinetics. This study demonstrates that laboratory experiments can successfully distinguish isotopic signatures arising from mass transport, chemical speciation, and electron transfer. Understanding how these processes fractionate metal isotopes under laboratory conditions is the first step towards discovering what role these processes play in fractionating metal isotopes in natural systems.

© 2010 Published by Elsevier Ltd.

1. INTRODUCTION

The role of electrochemical reactions, involving reduction or oxidation (redox) processes in fractionating the stable isotopes of transition metals is of growing interest for scientists working on a wide range of problems, such as understanding potential signatures of the origins of life

(Beard et al., 1999; Rouxel et al., 2005; Johnson et al., 2008), redox evolution in the solid Earth (Williams et al., 2004; Teng et al., 2008; Weyer, 2008), and remediation and environmental monitoring (Ellis et al., 2002; Rademacher et al., 2006). Explaining observed natural variations in the isotope record and using stable isotopes as markers for geochemical processes relies on a thorough understanding of the mechanisms controlling isotope partitioning as a result of the relevant physical phenomena. Here, we focus on the mechanisms underlying isotope fractionation in electron transfer reactions in Fe and Zn.

Electron transfer processes, also known as redox processes, are ubiquitous in nature, in aerosol chemistry, ocean

* Corresponding author. Tel.: +1 310 825 0173; fax: +1 310 825 2779.

E-mail addresses: jayblack@ucla.edu (J.R. Black), sjohn@gps.caltech.edu (S. John), eyoung@ess.ucla.edu (E.D. Young), akavner@ucla.edu (A. Kavner).

chemistry, weathering, biological processes, and element cycling between solid Earth, hydrosphere, biosphere, and atmosphere. The laboratory approach provides control of the thermodynamics and kinetics of the electron transfer process, allowing us to examine reaction rates spanning several orders of magnitude. The experimental approach enables us to examine isotope fractionation as a function of intensive variables of composition, and temperature and also as a function of thermodynamic driving force. The goal of this study is not to look at a single isotope system, nor a single geochemical process or application, but to establish the ground rules governing isotope fractionation during redox processes for all isotope systems.

In this study, we use Fe and Zn as test-systems for a variety of reasons. Iron is the most abundant transition metal, and its redox behavior in the solid Earth, hydrosphere, and biosphere has played an important role, including the establishment of complex life on this planet. Because of its interest in a variety of environmental settings it is one of the better-studied new transition metal stable isotope systems; however a predictive theory for its isotopic behavior across many processes is lacking. While in most natural environments Zn is not a redox-active element, compared with iron, its behavior during electroplating is more straightforward and its aqueous chemistry is much simpler to model. Zinc has several isotopes and high resolution techniques have been developed to examine its isotope fractionation. Any hypothesis that predicts iron isotope electrochemical behavior must predict zinc isotope behavior as well; therefore, zinc is an extremely useful cross check on our studies of iron. Ultimately, these studies will help establish theories predicting isotope behavior for all elements in all electrochemical processes.

The mechanisms underlying isotopic fractionation during a redox reaction are complex and can be governed by advective or diffusive mass transport, chemical speciation and reaction rates, and changes in phase associated with mineral precipitation (e.g., Anbar, 2004; Kavner et al., 2005). Much of the existing literature on isotopic self-exchange reactions between different redox states of an element have focused on determining the mass- and temperature dependence of equilibrium isotope fractionations among species from either first principles (Bigeleisen and Mayer, 1947; Urey, 1947) or from empirical constraints (Schauble et al., 2001; Anbar et al., 2005). Some experimental studies have determined the equilibrium fractionation between different transition metal redox states by monitoring fractionation during metal-oxide precipitation (Ellis et al., 2002; Johnson et al., 2002) or by examining isotopic equilibrium between dissolved species (Welch et al., 2003). These experiments have shown that both redox processes as well as changes in solution speciation play important roles in separating isotopes of transition metals. However, isotope fractionations much larger than those predicted by equilibrium stable isotope theory, where vibrational differences between isotopologue species drive isotope partitioning, have been observed during electroplating of metals (Kavner et al., 2005, 2008, 2009; Black et al., 2009a, 2010).

Kavner et al. (2005) combined stable isotope theory (Bigeleisen and Mayer, 1947; Urey, 1947) and electron transfer kinetics (Marcus, 1964, 1965) to predict a driving force-dependent isotope fractionation due to the electron transfer step. The theory predicts mass-dependent isotope fractionation in all systems which undergo electron transfer reactions. The theory was derived for a single electron transfer in a homogeneous system. Experimentally, voltage-dependent isotope separation is observed in electroplated iron (Kavner et al., 2005, 2009; Black et al., 2010), zinc (Kavner et al., 2008), and lithium (Black et al., 2009b) which conforms with theoretical predictions. We focus on the specific redox reaction of electroplating at an electrode because of the relative experimental simplicity of this system—reacted material can be easily separated, collected, and analyzed—and the control that we have over relevant variables, including thermodynamic driving force and kinetics, mass transport, and the extent of reaction. Results from iron studies (Kavner et al., 2009; Black et al., 2010) have suggested that mass transport-limited kinetics (i.e., diffusion to the electrode) attenuate what would otherwise be large isotope fractionations due to the electroplating process. In the experiments described by Kavner et al. (2009), large uncertainties existed in the electrochemical parameters, especially temperature, which was not controlled. The rotating disc electrode study (Black et al., 2010) confirmed the Kavner et al. (2009) result by showing that isotope fractionations of electrodeposited iron increase as a function of electrode rotation rate, which also serves to increase mass transport of Fe(II) reactant to the electrode. In addition, speciation-related isotope fractionation can occur in the double layer adjacent to the electrode and can contribute to the observed isotope signature. These processes are illustrated in Fig. 1, which depicts a cartoon of the molecular scale behavior at a charged electrode in solution. Fig. 1 summarizes the contributing processes determining the overall isotope signature of an electroplated metal: (1) isotope fractionation related to chemistry and speciation differences between the bulk solution, and across the double layer to the electrode ($\Delta^X M_{\text{Equilibrium}}$); (2) mass transport of material to the electrode, which includes mechanical mixing, diffusion, and electromigration ($\Delta^X M_{\text{MassTransport}}$); and (3) the electron transfer step itself ($\Delta^X M_{\text{Electrochemical}}$).

The goal of this study is to elucidate the contribution of each of these reaction steps towards the observed overall isotope signature of electroplating. Here, we examine isotope fractionation during the electrodeposition of both Fe and Zn to a planar electrode as a function of overpotential (defined as the difference between the applied voltage and the equilibrium voltage), time, temperature and stock solution chemistry. Using this experimental approach, we attempt to clarify which factors control isotopic fractionation and to quantify the magnitude of the isotope effects associated with different mechanisms of fractionation under different chemical conditions. The isotope effects measured in our experiments can be compared against natural isotope effects in order to better understand the processes which govern isotopic fractionation in nature.

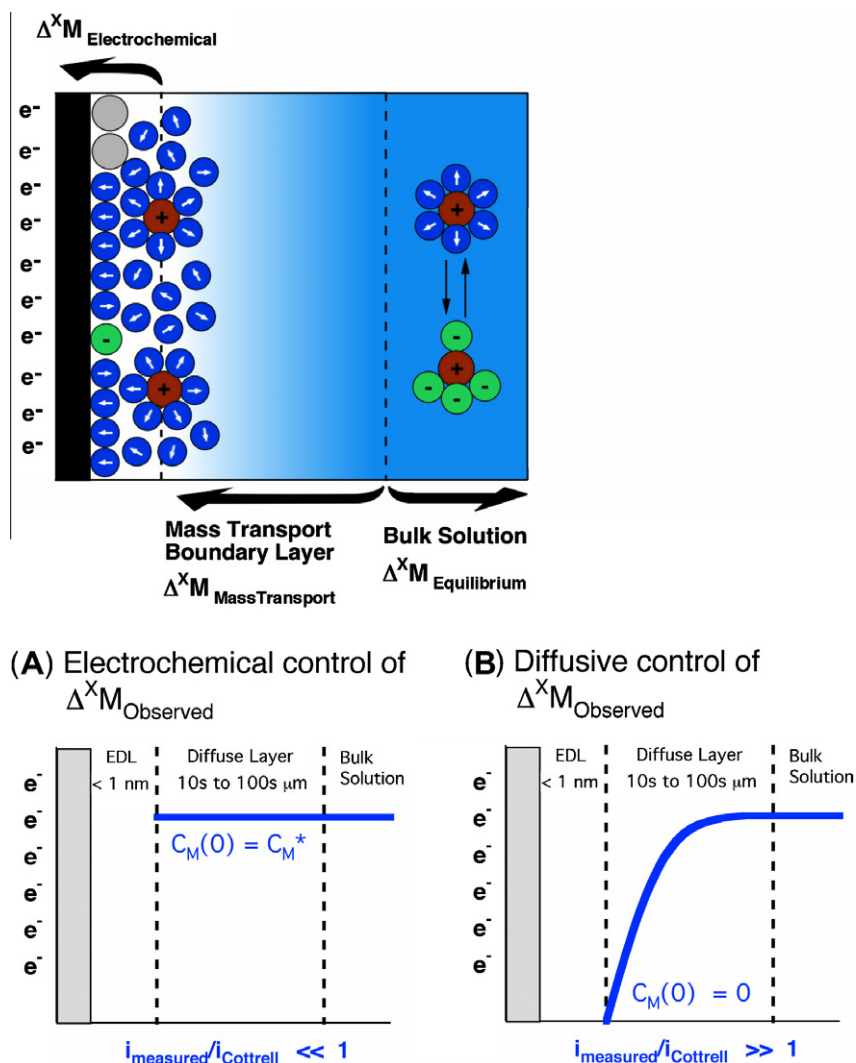


Fig. 1. Molecular scale behavior at a negatively charged electrode surface: initially there are specifically adsorbed species (e.g., water, blue spheres; chloride, green spheres) and aqueous metal complexes (e.g., iron, dark red spheres) at the surface in the electric double layer (EDL); as charge is transferred an electroplated metal film is deposited (gray spheres) on the electrode and a concentration gradient evolves (blue lines in (A) and (B)) in the mass transport boundary layer (diffuse layer) directly adjacent to the electrode. The potential processes inducing an isotopic fractionation are labeled next to the arrows. $C_M(0)$ is the concentration of oxidized aqueous metal at the electrode surface, and C_M^* is the bulk concentration in solution. (For interpretation of the references to color in this figure legend, the reader is referred to the web version of this article.)

2. EXPERIMENTAL METHODS

In all experiments, a small amount of metal (<0.1% of starting solution) was electroplated from aqueous metal salt plating solutions ($ZnSO_4$, $ZnCl_2$, $FeSO_4$ and $FeCl_2$, see Section 2.2) using a three-electrode cell under potentiostat control (Fig. 2). Plating experiments were performed as a function of a number of variables including the electrochemical overpotential, temperature, time (charge delivered), stir rate, cell geometry and electrode surface area. In each experiment, all of the plated material was collected from a glassy carbon electrode and the isotope composition was measured with respect to the starting solution, using high resolution MC-ICP-MS techniques.

2.1. Sample/stock preparation

Iron stock solutions were prepared by transferring a fixed amount of $FeCl_2 \cdot 2H_2O$ or $FeSO_4 \cdot 7H_2O$ (stored under argon) to the water-jacketed electrochemical cell (Fig. 2) and purged with argon gas. Degassed, doubly distilled water was then injected into the water-jacketed cell (cathodic cell 1, Fig. 2) via a septum to dissolve the iron in 90 mL. Half this solution was removed via the septum and 30 mL delivered to the secondary anodic cell (Fig. 2). Five milliliters was used to measure initial sample pH and 10 mL stored (for future analysis of concentrations) in a sample vial to which 1 mL of concentrated HCl or H_2SO_4 was added to help prevent oxidation of Fe(II) and precipitation of Fe(III) aqueous species. Zinc stock solutions were

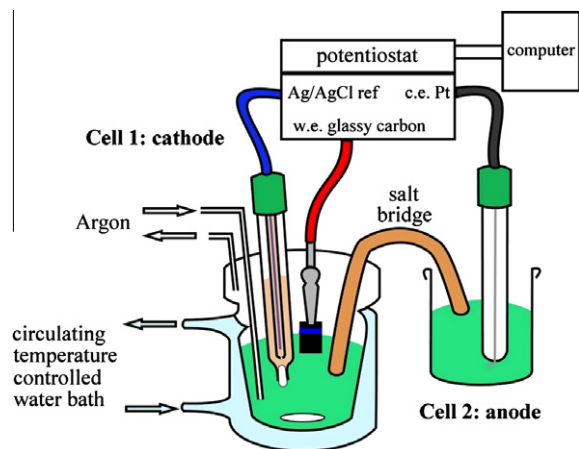


Fig. 2. Electrochemical cell schematic for the two-cell setup separated via a salt bridge.

prepared in 1–2 L batches from ZnSO_4 and ZnCl_2 salts and fresh aliquots were taken from these batch stocks for each separate experiment. See Table 1 for final stock solution compositions.

2.2. Potentiostatic electroplating

Electroplating voltage and time were controlled by an Autolab potentiostat (PGSTAT30) using a glassy carbon working electrode, a platinum counter electrode, and an Ag/AgCl double junction reference electrode (filled with 3 m KCl). A two-cell setup was used where the cathodic half cell and the anodic half cell were connected via a 2% (w/v) Agar in 4 m KCl salt bridge (16 cm \times 8 mm i.d.; Fig. 2). The working and reference electrodes were immersed in \sim 50 mL of degassed sample solution in cell 1 (Fig. 2) and the temperature of this solution was controlled by an external water bath. The counter electrode was placed in \sim 30 mL of sample solution in the anodic cell at room temperature. The equilibrium potential (E^0) of sample solutions in the two-cell setup was experimentally determined using cyclic voltammetry (CV) with variable sweep rates (Table 2). The junction potential of the salt bridge was determined by calibrating the Eh against ZoBell's solution (a mixture of aqueous $[\text{Fe}^{\text{II}}(\text{CN})_6]^{4-}$ and $[\text{Fe}^{\text{III}}(\text{CN})_6]^{3-}$, see ZoBell (1946) and Nordstrom (1977)) as a function of temperature (Wagman et al., 1982). In the following experiments electroplating overpotentials are reported relative to the experimentally determined values of E^0 (Fig. 3). The experimentally

Table 1
Stock solution composition and main experimental variables summary.

Experiment	Composition	pH	η range (V)	Temperature ($^{\circ}\text{C}$)	Speciation
Iron Experiment 01	0.78 M FeCl_2	2.5	–0.25 to –1.25	0, 25, and 35	$[\text{Fe}(\text{H}_2\text{O})_6]^{2+}_{(\text{aq})}$ (80%) $[\text{FeCl}]^+_{(\text{aq})}$ (20%)
Iron Experiment 02	0.46 M FeSO_4 + 0.04 M H_2SO_4	1.6	–0.5 to –1.0	0 and 25	$[\text{FeSO}_4]_{(\text{aq})}^0$ (50.8%) $[\text{Fe}(\text{H}_2\text{O})_6]^{2+}_{(\text{aq})}$ (36.7%) $[\text{FeHSO}_4]^+_{(\text{aq})}$ (12.5%)
Zinc Experiment 01	1 M ZnSO_4 + 1 M H_2SO_4	<1	–0.1 to –0.5	0, 25, and 50	$[\text{ZnSO}_4]_{(\text{aq})}^0$ (83%) $[\text{Zn}(\text{H}_2\text{O})_6]^{2+}_{(\text{aq})}$ (17%)
Zinc Experiment 02	1 M ZnSO_4	4.5	–0.025 to –0.4	0, 25, and 50	$[\text{ZnSO}_4]_{(\text{aq})}^0$ (93%) $[\text{Zn}(\text{H}_2\text{O})_6]^{2+}_{(\text{aq})}$ (7%)
Zinc Experiment 03	1 M ZnCl_2 in 6 M $[\text{Cl}]_{\text{tot}}$ as KCl	5.5	–0.14 to –0.4	25	$[\text{ZnCl}_4]^{2-}_{(\text{aq})}$ (60%) $[\text{ZnCl}_3]^-_{(\text{aq})}$ (14%) $[\text{ZnCl}_2]_{(\text{aq})}^0$ (11%) $[\text{ZnCl}]^+_{(\text{aq})}$ (7.5%) $[\text{Zn}(\text{H}_2\text{O})_6]^{2+}_{(\text{aq})}$ (7.5%)

Table 2
Summary of cyclic voltammetric determination of E^0 .

Temperature	Equilibrium potential, E^0 (V vs. Ag/AgCl in 3 m KCl E^0)			
	0 $^{\circ}\text{C}$	25 $^{\circ}\text{C}$	35 $^{\circ}\text{C}$	50 $^{\circ}\text{C}$
Iron Experiment 01	–0.607 V	–0.615 V	–0.629 V	
Iron Experiment 02	–0.560 V	–0.570 V		
Zinc Experiment 01	–1.093 V	–1.038 V		–1.002 V
Zinc Experiment 02	–1.018 V	–1.000 V		–0.984 V
Zinc Experiment 03		–1.033 V		
Calculated ^a (Wagman et al., 1982)				
$\text{Fe}^{2+} + 2\text{e}^- = \text{Fe}^{\text{(s)}}$	–0.663 V	–0.641 V	–0.633 V	
$\text{Zn}^{2+} + 2\text{e}^- = \text{Zn}^{\text{(s)}}$	–1.055 V	–1.029 V		–1.010 V

^a Calculated E^0 from known thermodynamic properties for species in the listed reactions.

determined E^0 values compare well to E^0 values calculated from the literature (Table 2), within ~ 1 – 10% (or ~ 10 mV).

A series of constant potential electroplating experiments were performed as a function of overpotential, time (Coulombs passed), temperature, and solution chemistry (see summary in Table 1). Additional experimental details, such as the initial surface area of glassy carbon working electrodes, solution stirring and total charge delivered, are presented in Table 3. After each experiment, the total amount of deposited material was monitored via dilutions (see next paragraph). Reaction currents are calculated via: $i_{\text{measured}} = nF/t$, where n is the amount of collected metal deposit (in moles), F is Faraday's constant = 96,485 C/mol, and t is the total time of the plating experiment (in seconds). The electroplating efficiency is given by the ratio of the calculated current (i_{measured}) to the total current ($i_{\text{average current}} = Q/t$ where Q is the total number of coulombs transferred in each experiment). Samples of the stock solution were obtained before and after reactions to ensure a constant isotope composition throughout the experiments (see Section 2.3).

To analyze iron, samples were dissolved in concentrated HCl in Teflon cups and evaporated down until a sparing amount of solution was left to which 5 mL of 2% (w/v) HNO_3 was added. Samples were then diluted to a final concentration of 1 ppm for isotopic analyses (see Section 2.3). Samples of electroplated zinc were dissolved in 2% HNO_3 in Teflon cups and evaporated to dryness and diluted with 5 mL of 2% HNO_3 . Before isotopic analysis (see Section 2.3) the samples were diluted to a final concentration of 20 ppm. Concentrations of metal in final dilutions were measured to provide an estimate of the total amount of metal electroplated.

2.3. Isotopic analysis

2.3.1. Iron

Isotopic analyses were performed using a Thermo-Finnigan Neptune Multi-collector Inductively Coupled Plasma Mass Spectrometer (MC-ICP-MS) housed at UCLA. An Aridus desolvating nebuliser was used for measurement in high resolution mode with signal intensities for ^{54}Fe , ^{56}Fe and ^{57}Fe monitored on cups L1, C and H1, respectively. A standard-sample bracketing technique was used, with 1 ppm Spex1 (an in-house standard diluted from a 1000 ppm iron stock). At the beginning of each session measurements of two separate Spex1 standards were collected to ensure a low zero-enrichment ($0.00 \pm 0.07\text{‰} - 2\sigma$). Sample replicates of 20 cycles with a 4-s integration per cycle were collected, with three to five bracketed replicates collected per sample. Sample cycle measurements that lay outside 2σ of the mean were excluded as outliers. A measurement of the international standard IRMM-14 was collected before and after the sample replicates to monitor instrumental drift relative to the in-house standard Spex1. Table 4 presents the detailed isotopic results of iron metal deposits and stock solutions including the long term reproducibility of the standards (Spex1 and IRMM-14).

2.3.2. Zinc

Isotopic analyses were performed using a Thermo-Finnigan Neptune Multi-collector Inductively Coupled Plasma Mass Spectrometer at Caltech. Samples were introduced via a cyclonic spray chamber. All samples and standards were diluted to a Zn concentration of 20 ppm and spiked with 20 ppm of an in-house Cu standard. Samples were run alternately with a NIST SRM 682 standard, also spiked with Cu, which has previously been compared to JMC 3-0749L Zn (John et al., 2007). Signal intensity on ^{60}Ni , ^{63}Cu , ^{64}Zn , ^{65}Cu , ^{66}Zn , and ^{68}Zn were monitored on cups L3, L2, L1, C, H1, and H2, respectively. Samples and standards were run alternately for 3 min each, with 3 min rinsing in between. The intensity of ^{60}Ni was used to correct for an interference of ^{64}Ni on ^{64}Zn , after estimating instrumental mass bias from the Cu isotope ratio, though these corrections were always insignificant. Monitoring of the measured Cu isotope ratio in samples showed that there was no significant mass bias due to matrix effects in samples compared to standards. All samples were therefore corrected for instrumental mass bias using only sample-standard bracketing, which slightly improves precision by eliminating the analytical error associated with measuring Cu isotopes. Each sample was measured at least three times. Table 5 presents the detailed isotopic compositions of samples of electroplated zinc metal and stock solutions.

In all experiments the isotopic composition of the stock solution was unchanged within experimental error before and after an electroplating experiment. This establishes a constant isotope reservoir, with no effects from salt bridge migration or Rayleigh-type compositional evolution.

3. RESULTS

The isotopic composition of the electrodeposited materials with respect to their stock solutions are summarized in Table 3 and shown in Fig. 4 (Iron) and Fig. 5 (Zinc). All electroplated samples were isotopically lighter than their stock solutions and follow mass-dependent fractionation laws (Tables 4, 5 and Fig. 6). Fractionations as large as $\Delta^{56}\text{Fe}_{\text{sample-stock}} = -4.1\text{‰}$ (sample Fe02_01, Table 3) and $\Delta^{66}\text{Zn}_{\text{sample-stock}} = -5.5\text{‰}$ (Zn01_10, Table 3) are observed. These values demonstrate that electroplating provides the largest single-pass isotope separations yet observed for iron and zinc.

At constant temperature, the magnitude of fractionation of both iron and zinc isotopes during metal deposition on planar electrodes decreases with increasing overpotential (Figs. 4A and 5A). The magnitude of the negative slope varies depending upon the starting solution composition, e.g., the slope is $\sim -0.9\text{‰ V}^{-1}$ for $\text{Fe}_{(\text{s})}$ plated from 0.8 M FeCl_2 and -6 for $\text{Fe}_{(\text{s})}$ plated from 0.5 M FeSO_4 .

At a constant overpotential, isotope fractionations were observed to increase as a function of temperature (Figs. 4A and 5A). However, the extent of the temperature dependence of fractionation depends on solution chemistry. FeCl_2 has a strong positive temperature dependence while FeSO_4 has a weak negative dependence. The acidic ZnSO_4 solutions show a strong positive temperature dependence, but there is little if any dependence seen in neutral ZnSO_4

Table 3
Summary of electrochemical experiments and MC-ICP-MS results.

Sample	Temperature (°C)	η^a (V)	Stir rate (rpm)	Charge delivered (C)	Average current (mA)	Electrode surface area (mm ²)	Cottrell diffusion-limiting current (mA)	Efficiency ^b (%)	$\Delta^{56}\text{Fe}$ (‰) $\pm 2\sigma^c$ $\Delta^{66}\text{Zn}$ (‰) $\pm 2\sigma^d$	N^e
Iron experiments										
<i>Experiment 01</i>										
Fe01_01	0.2	-0.50	200	20	-36.08	217	-20.99	89	-1.67 \pm 0.07	5
Fe01_02	0.2	-0.75	200	20	-93.68	230	-35.84	101	-1.33 \pm 0.08	5
Fe01_03	0.5	-1.00	200	20	-140.75	209	-39.92	99	-1.26 \pm 0.09	5
Repeat ⁱ										
Fe01_04	0.5	-1.25	200	20	-199.80	183	-41.56	95	-0.88 \pm 0.10	3
Fe01_05	25	-0.25	200	5	-0.92	230	-8.26	12	-2.03 \pm 0.09	5
Fe01_06	25.2	-0.50	200	20	-87.91	211	-31.87	101	-1.80 \pm 0.17	3
Repeat ⁱ										
Fe01_07	25	-0.50	200	20	-81.97	213	-31.05	94	-1.86 \pm 0.09	4
Fe01_08	25.8	-0.75	200	5	-156.25	–	-92.58	90	-1.67 \pm 0.07	5
Fe01_09	25	-0.75	200	20	-180.67	197	-42.55	90	-1.62 \pm 0.07	5
Fe01_10	25	-0.75	200	50	-175.87	209	-28.16	78	-1.71 \pm 0.08	5
Fe01_11 ^f	25	-0.75	200	20	-153.37	226	-52.58	91	-1.75 \pm 0.10	5
Fe01_12	25	-0.75	None	20	-159.74	230	-54.60	94	-1.13 \pm 0.08	5
Fe01_13	25.2	-1.00	200	20	-254.78	208	-53.46	89	-1.36 \pm 0.08	5
Fe01_14	35	-0.25	200	20	-11.69	220	-12.08	80	-2.17 \pm 0.10	3
Fe01_15	35	-0.50	200	20	-65.06	204	-26.44	94	-2.19 \pm 0.08	5
Repeat ⁱ										
Fe01_16	35	-0.75	200	20	-161.03	210	-42.87	73	-1.77 \pm 0.09	5
Fe01_17	35	-0.97	200	20	-271.00	230	-60.96	74	-1.62 \pm 0.10	5
<i>Experiment 02</i>										
Fe02_01	0.5	-0.50	200	20	-7.07	219	-5.61	0.1	-4.13 \pm 0.32	5
Repeat ⁱ										
Fe02_02	0.5	-0.75	200	20	-21.23	–	-10.21	12	-2.59 \pm 0.10	3
Fe02_03	0.5	-0.84	200	20	-42.11	230	-12.91	8	-1.57 \pm 0.06	5
Fe02_04	25.5	-0.50	200	20	-19.67	230	-9.83	0.6	-3.82 \pm 0.10	5
Fe02_05	25	-0.75	200	20	-40.29	212	-12.99	5	-2.18 \pm 0.10	4
Fe02_06	25	-0.77	200	20	-48.44	220	-28.69	6	-2.77 \pm 0.06	5
Fe02_07	25.8	-1.00	200	20	-47.43	183	-23.62	38	-1.62 \pm 0.21	5
Repeat ⁱ										
<i>Zinc experiments</i>										
<i>Experiment 01</i>										
Zn01_01	0.5	-0.119	200	20	-30.67	245	-22.67	44	-4.65 \pm 0.11	3
Zn01_02	0.3	-0.219	200	20	-74.27	204	-29.37	79	-4.17 \pm 0.10	5
Zn01_03	0.5	-0.319	200	20	-125.63	245	-45.88	73	-4.08 \pm 0.07	3
Repeat ⁱ										
Zn01_04	24.2	-0.114	200	20	-33.49	236	-22.82	26	-5.14 \pm 0.08	3
Zn01_05	25	-0.114	200	20	-35.55	225	-22.41	44	-4.97 \pm 0.09	3
Zn01_06	24.5	-0.214	200	20	-100.65	224	-37.55	91	-4.46 \pm 0.07	5
Zn01_07	25	-0.314	200	20	-154.32	225	-46.70	86	-4.27 \pm 0.08	3
Zn01_08	24.5	-0.514	200	20	-275.86	226	-62.71	92	-3.93 \pm 0.06	3
Zn01_09	50	-0.138	200	20	-64.29	263	-35.23	61	-5.45 \pm 0.07	3
Zn01_10	50	-0.238	200	20	-144.61	236	-47.42	93	-5.50 \pm 0.07	5
Zn01_11	50	-0.338	200	20	-246.31	220	-57.69	93	-4.70 \pm 0.07	3
Repeat ⁱ										
<i>Experiment 02</i>										
Zn02_01	0.5	-0.032	200	20	-5.46	202	-7.90	100	-3.10 \pm 0.10	3
Zn02_02	0.1	-0.132	200	20	-12.99	183	-11.00	98	-3.45 \pm 0.10	3
Zn02_03	0.1	-0.232	200	20	-23.50	219	-17.74	57	-2.96 \pm 0.08	3
Zn02_04	25.2	-0.076	200	20	-11.36	214	-12.02	98	-3.33 \pm 0.09	3
Zn02_05 ^g	25	-0.176	200	20	-30.08	228	-20.88	100	-3.16 \pm 0.09	3
Zn02_06 ^g	26	-0.176	200	20	-37.38	230	-23.50	105	-3.22 \pm 0.09	3
Zn02_07	26.1	-0.176	200	20	-15.67	54	-3.57	109	-3.42 \pm 0.09	3
Zn02_08	25	-0.276	200	20	-39.14	207	-21.64	97	-3.27 \pm 0.09	3
Zn02_09 ^h	25.7	-0.376	200	20	-5.14	215	-8.15	97	-3.82 \pm 0.09	3
Zn02_10	50	-0.120	200	20	-7.91	217	-10.19	99	-3.19 \pm 0.09	3

Table 3 (continued)

Sample	Temperature (°C)	η^a (V)	Stir rate (rpm)	Charge delivered (C)	Average current (mA)	Electrode surface area (mm ²)	Cottrell diffusion-limiting current (mA)	Efficiency ^b (%)	$\Delta^{56}\text{Fe}$ (‰) $\pm 2\sigma^c$ $\Delta^{66}\text{Zn}$ (‰) $\pm 2\sigma^d$	N^e
Zn02_11	50	-0.220	200	20	-12.93	215	-12.93	100	-3.51 \pm 0.08	3
Zn02_12	50	-0.320	200	20	-39.60	230	-24.18	101	-3.09 \pm 0.09	3
<i>Experiment 03</i>										
Zn03_01	25.5	-0.140	200	20	-42.76	234	-25.61	99	-3.01 \pm 0.09	3
Zn03_02	25.5	-0.190	200	20	-81.00	209	-31.43	97	-2.80 \pm 0.09	3
Zn03_03	25	-0.290	200	20	-151.75	241	-49.60	102	-2.80 \pm 0.08	3
Zn03_04	25.5	-0.340	200	20	-211.64	241	-58.58	104	-2.72 \pm 0.07	3
Zn03_05	25	-0.390	200	20	-283.69	217	-61.06	102	-2.44 \pm 0.07	3

^a Overpotential, η , ($E - E^0$) relative to measured E^0 from CV spectra (Table 2, Fig. 3).

^b Percentage yield of metal plated (measured using AAS or ICP-MS) relative to the theoretical mass expected from charge delivered.

^c The isotopic composition of the samples is expressed as a per-mil deviation from the stock solution: in the case of iron experiments: $\Delta^{56}\text{Fe} = \delta^{56}\text{Fe}_{\text{sample}} - \delta^{56}\text{Fe}_{\text{stock}}$, where $\delta^{56}\text{Fe} = [({}^{56}\text{Fe}/{}^{54}\text{Fe})_{\text{sample}}/({}^{56}\text{Fe}/{}^{54}\text{Fe})_{\text{Spex1}} - 1] * 1000$.

^d The isotopic composition of the samples is expressed as a per-mil deviation from the stock solution: in the case of zinc experiments: $\Delta^{66}\text{Zn} = \delta^{66}\text{Zn}_{\text{sample}} - \delta^{66}\text{Zn}_{\text{stock}}$, where $\delta^{66}\text{Zn} = [({}^{66}\text{Zn}/{}^{64}\text{Zn})_{\text{sample}}/({}^{66}\text{Zn}/{}^{64}\text{Zn})_{\text{NIST}} - 1] * 1000$.

^e N = number of replicate measurements.

^f Only one cell used, no salt bridge.

^g Test of cell geometry: changing position of working electrode relative to counter and reference electrodes in solution.

^h Change in cell geometry, working electrode further from counter and reference electrodes in solution.

ⁱ Repeat signifies a repeat analysis of the above sample but during a separate analytical session.

Table 4

Iron stable isotope fractionation of electroplated iron on planar glassy carbon electrodes.

Sample	$\delta^{56}\text{Fe}^a$ (‰) $\pm 2\sigma$	$\delta^{57}\text{Fe}^a$ (‰) $\pm 2\sigma$	N^b	Sample	$\delta^{56}\text{Fe}^a$ (‰) $\pm 2\sigma$	$\delta^{57}\text{Fe}^a$ (‰) $\pm 2\sigma$	N^b
<i>Experiment 01</i>				<i>Experiment 02</i>			
Fe01_03_Stk ^c	0.667 \pm 0.022	0.981 \pm 0.076	3	Fe02_01_Stk ^f	0.583 \pm 0.035	0.884 \pm 0.082	3
Fe01_06_Stk ^c	0.625 \pm 0.051	0.904 \pm 0.141	5	Fe02_05_Stk ^f	0.608 \pm 0.092	0.901 \pm 0.131	5
Fe01_06_Cell1 ^d	0.680 \pm 0.031	0.994 \pm 0.062	3	Fe02_06_Stk ^g	0.843 \pm 0.040	1.232 \pm 0.049	5
Fe01_15_Stk ^c	0.659 \pm 0.041	0.945 \pm 0.058	5	Fe02_06_Cell1	0.846 \pm 0.023	1.268 \pm 0.097	5
Fe01_15_Cell1 ^d	0.640 \pm 0.052	0.922 \pm 0.089	5	Fe02_01	-3.529 \pm 0.302	-4.985 \pm 0.294	5
Fe01_01	-1.021 \pm 0.021	-1.514 \pm 0.047	5	Repeat ^h	-3.329 \pm 0.054	-4.809 \pm 0.126	3
Fe01_02	-0.679 \pm 0.030	-1.064 \pm 0.108	5	Fe02_02	-1.992 \pm 0.036	-2.748 \pm 0.084	3
Fe01_03	-0.609 \pm 0.055	-0.943 \pm 0.074	5	Fe02_03	-0.725 \pm 0.039	-1.083 \pm 0.037	5
Repeat ^h	-0.506 \pm 0.055	-0.780 \pm 0.114	3	Fe02_04	-3.224 \pm 0.019	-4.787 \pm 0.035	5
Fe01_04	-0.232 \pm 0.069	-0.406 \pm 0.127	3	Fe02_05	-1.584 \pm 0.023	-2.379 \pm 0.127	4
Fe01_05	-1.380 \pm 0.055	-2.064 \pm 0.164	5	Fe02_06	-1.926 \pm 0.039	-2.874 \pm 0.095	5
Fe01_06	-1.148 \pm 0.155	-1.727 \pm 0.179	3	Fe02_07 ^e	-1.025 \pm 0.184	-1.554 \pm 0.157	5
Repeat ^h	-1.092 \pm 0.051	-1.605 \pm 0.074	5	Repeat ^h	-1.080 \pm 0.018	-1.619 \pm 0.113	3
Fe01_07	-1.210 \pm 0.057	-1.854 \pm 0.083	5	<i>Standards</i>			
Fe01_08	-1.014 \pm 0.022	-1.523 \pm 0.112	5	Spex1	0	0	
Fe01_09	-0.967 \pm 0.020	-1.438 \pm 0.047	5	IRMM-014	0.225 \pm 0.051	0.318 \pm 0.095	54
Fe01_10	-1.056 \pm 0.042	-1.607 \pm 0.129	5				
Fe01_11	-1.097 \pm 0.074	-1.674 \pm 0.039	5				
Fe01_12	-0.475 \pm 0.043	-0.705 \pm 0.122	5				
Fe01_13	-0.710 \pm 0.035	-1.051 \pm 0.059	5				
Fe01_14	-1.517 \pm 0.071	-2.235 \pm 0.075	3				
Fe01_15	-1.539 \pm 0.045	-2.338 \pm 0.051	5				
Repeat ^h	-1.494 \pm 0.100	-2.245 \pm 0.115	3				
Fe01_16	-1.123 \pm 0.052	-1.624 \pm 0.050	5				
Fe01_17	-0.971 \pm 0.073	-1.458 \pm 0.062	5				

^a The isotopic composition of the samples is expressed as a per-mil deviation from the Spex1 standard using the formula: $\delta^x\text{Fe} = [({}^x\text{Fe}/{}^{54}\text{Fe})_{\text{sample}}/({}^x\text{Fe}/{}^{54}\text{Fe})_{\text{Spex1}} - 1] * 1000$.

^b N = number of standard bracketed replicates (20 cycles each).

^c Stk = initial stock solution.

^d Cell1 = final stock solution.

^e Sample acidified with HCl instead of H₂SO₄.

^f Stocks prepared from different FeSO₄·7H₂O sources.

^g Stocks prepared from different FeSO₄·7H₂O sources.

^h Repeat signifies a repeat analysis of the above sample but during a separate analytical session.

Table 5

Zinc stable isotope fractionation of electroplated zinc on planar glassy carbon electrodes.

Sample	$\delta^{66}\text{Zn}^a$ (‰) $\pm 2\sigma$	$\delta^{68}\text{Zn}^a$ (‰) $\pm 2\sigma$	N^b	Sample	$\delta^{66}\text{Zn}^a$ (‰) $\pm 2\sigma$	$\delta^{68}\text{Zn}^a$ (‰) $\pm 2\sigma$	N^b
<i>Experiment 01</i>				<i>Experiment 02</i>			
Zn01_Stk ^c	2.732 \pm 0.056	5.443 \pm 0.215	5	Zn02_Stk ^c	2.685 \pm 0.042	5.301 \pm 0.149	3
Zn01_Stk ^c	2.741 \pm 0.055	5.455 \pm 0.157	5	Zn02_Stk ^c	2.633 \pm 0.123	5.267 \pm 0.256	3
Zn01_01_Cell1 ^d	2.666 \pm 0.040	5.306 \pm 0.185	3	Zn02_04_Cell1 ^d	2.664 \pm 0.070	5.289 \pm 0.155	3
Zn01_05_Cell1 ^d	2.848 \pm 0.039	5.438 \pm 0.129	5	Zn02_01	-0.437 \pm 0.052	-0.944 \pm 0.117	3
Zn01_07_Cell1 ^d	2.442 \pm 0.132	4.787 \pm 0.256	3	Zn02_02	-0.793 \pm 0.056	-1.594 \pm 0.222	3
Repeat ^e	2.657 \pm 0.039	5.333 \pm 0.083	3	Zn02_03	-0.301 \pm 0.014	-0.587 \pm 0.104	3
Zn01_09_Cell1 ^d	2.619 \pm 0.022	4.891 \pm 0.032	3	Zn02_04	-0.672 \pm 0.040	-1.332 \pm 0.024	3
Zn01_01	-1.911 \pm 0.100	-3.834 \pm 0.206	3	Zn02_05	-0.505 \pm 0.043	-0.946 \pm 0.159	3
Zn01_02	-1.433 \pm 0.077	-2.796 \pm 0.297	5	Zn02_06	-0.562 \pm 0.045	-1.115 \pm 0.142	3
Zn01_03	-1.341 \pm 0.045	-2.709 \pm 0.352	3	Zn02_07	-0.761 \pm 0.027	-1.485 \pm 0.049	3
Repeat ^e	-1.303 \pm 0.007	-2.567 \pm 0.026	3	Zn02_08	-0.610 \pm 0.028	-1.137 \pm 0.129	3
Zn01_04	-2.406 \pm 0.059	-4.761 \pm 0.205	3	Zn02_09	-1.158 \pm 0.023	-2.209 \pm 0.033	3
Zn01_05	-2.235 \pm 0.067	-4.419 \pm 0.154	3	Zn02_10	-0.527 \pm 0.044	-0.883 \pm 0.131	3
Zn01_06	-1.724 \pm 0.036	-3.361 \pm 0.124	5	Zn02_11	-0.855 \pm 0.018	-1.662 \pm 0.084	3
Zn01_07	-1.537 \pm 0.052	-2.946 \pm 0.207	3	Zn02_12	-0.428 \pm 0.022	-0.829 \pm 0.078	3
Zn01_08	-1.193 \pm 0.016	-2.246 \pm 0.111	3	<i>Experiment 03</i>			
Zn01_09	-2.716 \pm 0.050	-5.333 \pm 0.079	3	Zn03_Stk ^c	2.672 \pm 0.051	5.426 \pm 0.125	3
Zn01_10	-2.763 \pm 0.046	-5.430 \pm 0.162	5	Zn03_02_Cell1 ^d	2.652 \pm 0.048	5.385 \pm 0.153	3
Zn01_11	-1.961 \pm 0.046	-3.879 \pm 0.291	3	Zn03_01	-0.335 \pm 0.071	-0.594 \pm 0.256	3
Repeat ^e	-1.967 \pm 0.057	-3.889 \pm 0.119	3	Zn03_02	-0.132 \pm 0.072	-0.211 \pm 0.291	3
<i>Standards</i>				Zn03_03	-0.126 \pm 0.061	-0.171 \pm 0.175	3
NIST	0	0		Zn03_04	-0.043 \pm 0.044	-0.048 \pm 0.071	3
A-20K	-6.709 \pm 0.075	-13.254 \pm 0.267	39	Zn03_05	0.232 \pm 0.050	0.479 \pm 0.040	3

^a The isotopic composition of the samples is expressed as a per-mil deviation from the Spex1 standard using the formula: $\delta^x\text{Zn} = [(^x\text{Zn}/^{64}\text{Zn})_{\text{sample}} / (^x\text{Zn}/^{64}\text{Zn})_{\text{NIST}} - 1] * 1000$.

^b N = number of standard bracketed replicates (30 cycles each).

^c Stk = initial stock solution.

^d Cell1 = final stock solution.

^e Repeat signifies a repeat analysis of the above sample but during a separate analytical session.

solutions. The temperature effect is distinct from a reaction current effect. At constant temperature, fractionation decreases as reaction current increases. At constant overpotential, increased temperature increases reaction current, however in this case, isotope fractionation increases. Therefore, opposite trends in fractionation as a function of current are observed, and a single current-driven fractionation model cannot explain the observed fractionations as a function of temperature and overpotential.

A series of experiments were performed to test the isotope sensitivity of various aspects of the experimental design and the electrochemical cell geometry, to determine which experimental variables may be important for isotope fractionation and which are not. At a single overpotential and temperature, no significant changes in fractionation are observed as a function of charge passed from 5 to 50 C (see samples Fe01_08 to Fe01_10, Table 3) over a time range of 32–284 s. This indicates that the fractionation does not change with time, as long as the electrodeposition rate is held constant. We observed no difference in the measured fractionation using a dual-cell/salt bridge geometry and a single cell geometry (see samples Fe01_09 and Fe01_11, Table 3). Other changes in cell geometry, such as the position of the working electrode relative to the counter and reference electrodes, affected the magnitude of current measured, but not the measured fractionation in samples (see samples Zn02_05 and Zn02_06, Table 3). The area of work-

ing electrode exposed had a large effect on the overall current, and thus time taken to deliver a fixed number of Coulombs of charge, with lower average currents being passed (-16 mA vs. -30 mA) with less working electrode surface exposed to the stock solution (54 mm² vs. 228 mm² in samples Zn02_05 and Zn02_07, respectively, Table 3). However, this only had a small effect on the fractionation between solution and the plated metal, i.e., ~0.26‰ difference in composition between samples Zn02_05 and Zn02_07. In most cases the experimental cell geometry was kept as consistent as possible in order to examine both fractionation and current trends between samples. Tests of the stock solution composition before and after an experiment show that the isotope composition of the stock remains unchanged (Tables 4 and 5).

On the other hand, stirring stock solutions during electroplating with a magnetic stir bar did affect the overall observed isotope fractionation, with much larger fractionations seen in stirred samples, e.g., iron: sample Fe01_09 (stirred, Table 3) is ~0.5‰ lighter than sample Fe01_12 (unstirred, Table 3); zinc: stirred samples in Zn Exp. 01 (Table 3) are ~2‰ lighter than samples plated from similar unstirred stock solutions used in previous studies (Fig. 5A, Kavner et al., 2008). This result is in accordance with the importance of the mass transport influence on isotope fractionation, as described in Section 4.

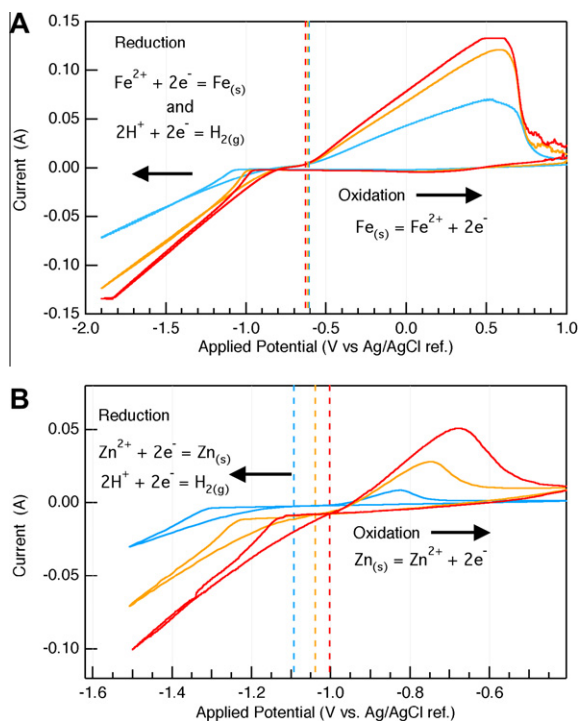


Fig. 3. Cyclic voltammetry as a function of temperature (0 °C: blue; 25 °C: orange; 35 °C –Fe/50 °C –Zn: red) for (A) 0.8 M FeCl_2 stock solutions; (B) 1 M ZnSO_4 in 1 M H_2SO_4 stock solutions. The position of the E^0 for metal deposition as a function of temperature is shown as dashed lines at fixed overpotentials. (For interpretation of the references to color in this figure legend, the reader is referred to the web version of this article.)

A plot of the fractionation on a three-isotope plot shows the nature of the mass dependency of the isotope fractionation. Following the approach of Young and Galy (2004), we plot $\Delta^X M'$ vs. $\delta^Y M'$ for iron ($X = 56/54$, $Y = 57/54$, Fig. 6A) and zinc ($X = 66/64$, $Y = 68/64$, Fig. 6B) where $\Delta^X M' = \delta^X M' - \beta_{\text{equilibrium}} \cdot \delta^Y M'$ and $\beta_{\text{equilibrium}} = ((1/m_1 + 1/m_2)/(1/m_1 + 1/m_3))$. By definition, an isotope fractionation due to equilibrium processes generates a line with slope zero. A non-zero slope on this plot implies that kinetic processes are underlying the isotope fractionation (Young et al., 2002). Weighted best fit lines through our data sets yield slopes of -0.00292 ± 0.00115 for iron and -0.01049 ± 0.00057 for zinc (2σ). Using the atomic masses of iron and zinc isotopes, the calculated kinetic slopes are -0.00594 and -0.00757 , respectively. Using the molecular weights of hexaquo complexes—likely to be representative of the predominant species in our solution—kinetic fractionation slopes are calculated to be -0.00954 for iron and -0.01202 for zinc. Although the measured slope for zinc is in good agreement with calculated kinetic slopes, the iron slope is much lower, suggesting that a combination of equilibrium and kinetic processes are causing the fractionation for iron.

4. DISCUSSION

These results are somewhat different from previous studies of isotope fractionation during electroplating. For

example, Kavner et al., 2005, observed that iron fractionation increases with increasing driving force—opposite the trend observed in this data set (Fig. 4A). For zinc, although the trends of fractionation vs. voltage are similar, we observe a much larger magnitude of fractionation compared with an earlier study (Kavner et al., 2008). Although the goal of the experiments were the same—to measure isotope fractionations during electroplating—small differences in the design of the experiments show significant variations in the isotope behavior at the electrode.

A first significant difference is in the earlier set of iron experiments (Kavner et al., 2005) the efficiency of the iron plating reaction with respect to hydrogen evolution was about an order of magnitude smaller (average $\sim 2 \pm 5\%$) than in the current experiments (average efficiency of $\sim 90 \pm 17\%$ for Fe Exp. 01, Table 3). We attribute this difference to the lower pH of stock solutions leading to an increase in $\text{H}_{2(\text{g})}$ production at the working electrode. The result was a plating reaction with very low efficiency compared with the total reaction current. However, within this current data set, we do not observe any systematic trend in the fractionation of samples as a function of the plating efficiency (Table 3). A second significant difference is that no temperature control was attempted in first sets of experiments (Kavner et al., 2005, 2008). Electroplating is highly exothermic, and our measurements show that the temperature of the plating solution rises at about 1 deg/min in the absence of temperature control. The other significant difference is that the solution was stirred in the current set of experiments, but not in the first sets of experiments. In the first sets of experiments, this was not considered an issue, because the observed bubbling at the electrode (because of H_2 evolution) was assumed to mix the solution adjacent to the electrode.

This set of experiments shows clearly that isotope separation at an electrode is quite sensitive to minor variations in experimental protocol. This variation also provides a means to evaluate different processes that might cause fractionation at an electrode. These were illustrated in Fig. 1 in Section 1 and the following sections examine the individual contributions to the overall observed fractionation. Our approach in this paper is to examine each of these fractionation mechanisms—speciation effects, mass transport, and electrochemistry. As a starting point, we iterate through each mechanism, evaluating their contributions to the fractionation observed and potential interaction. Ultimately, our goal is to perform a more sophisticated reservoir model of the behavior at the electrode, taking multiple mechanisms into account. We consider our current approach to be a necessary preliminary step.

4.1. Speciation and equilibrium effects

Isotope fractionation can result between two different aqueous species, just from equilibrium considerations. In this section, we consider equilibrium fractionation between species in the bulk solution and the metal precipitate and also the possibility that the isotopic composition of the species just adjacent to the electrode may be different, in general from the bulk. The bulk speciation in stock solutions

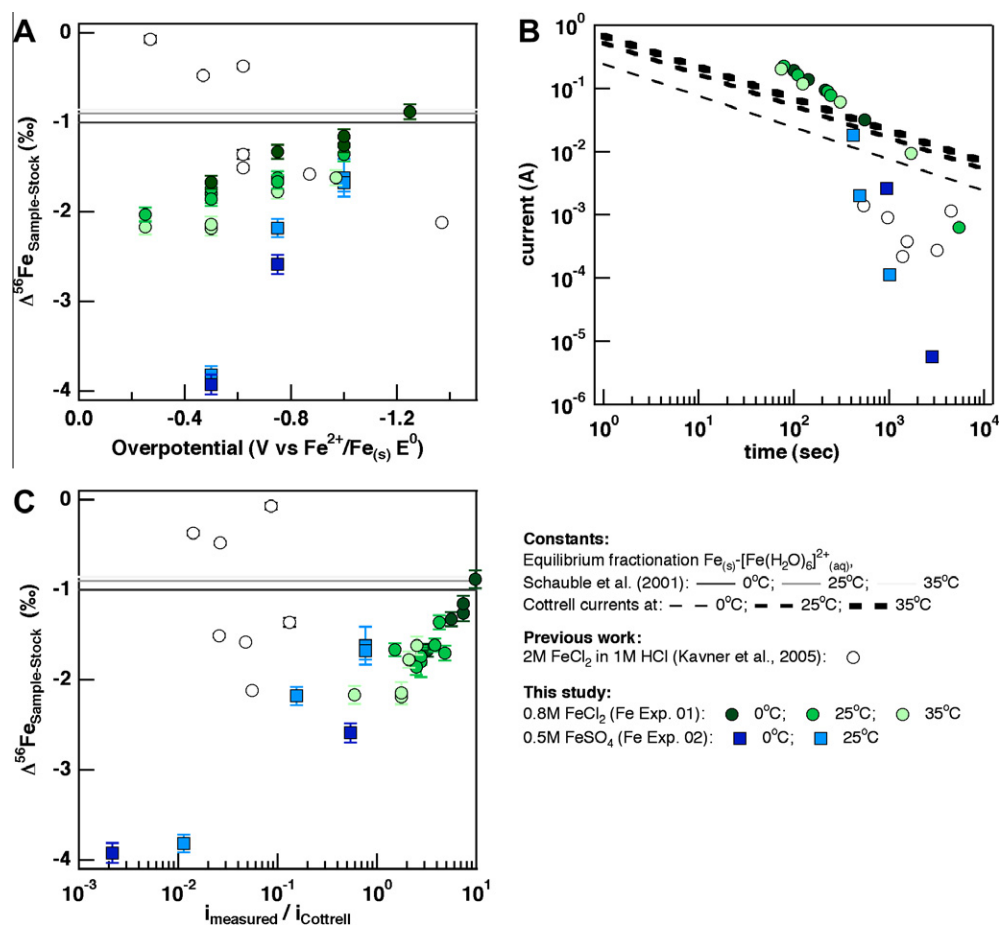


Fig. 4. Results from iron experiments showing: (A) $\Delta^{56}\text{Fe}$ vs. overpotential; (B) effect of temperature on the diffusion-limiting Cottrell current calculated for 0.78 M stock solution of iron (dashed lines) with experimental current superimposed; (C) $\Delta^{56}\text{Fe}$ vs. the ratio of experimental current to Cottrell diffusion-limiting current.

described in Section 2.1 is summarized in Table 1. The bulk chemistry of iron chloride stock solutions was calculated from thermodynamic properties (Heinrich and Seward, 1990; Parkhurst, 1995; Liu et al., 2007) and the speciation calculation shows that $[\text{Fe}(\text{H}_2\text{O})_6]^{2+}_{(aq)}$ is predominant (80%) with some $[\text{FeCl}]^+_{(aq)}$ forming (20%). Both these species are positively charged and are likely to be attracted to and interact with the negatively charged electrode surface. The speciation in iron sulfate solutions (Parkhurst, 1995) is a little more complex with a mixture of species forming: $[\text{Fe}(\text{H}_2\text{O})_6]^{2+}_{(aq)}$ (36.7%), $[\text{FeSO}_4]_{(aq)}$ (50.8%) and $[\text{FeHSO}_4]^+_{(aq)}$ (12.5%) at a pH of 1.6. In the case of Zn, thermodynamic models (Parkhurst, 1995; Liu et al., 2007; Ninkovic et al., 2007) of Zn speciation show that the $[\text{ZnSO}_4]_{(aq)}$ complex is predominant in the bulk solution of the sulfate experiments (Zn Exp. 01 and Zn Exp. 02), and spectroscopic studies (Rudolph et al., 1999) show that there is an equilibrium between outer-sphere and inner-sphere zinc-sulfate complexes. In the case of the Zn chloride experiments (Zn Exp. 03) a $[\text{ZnCl}_4]^{2-}_{(aq)}$ complex predominates the aqueous speciation in bulk solution.

Speciation at the charged electrode surface will differ dramatically from speciation in bulk solution (Epelboin

et al., 1975; Grujicic and Pesic, 2005; Diaz et al., 2008), with changes in chemistry, pH, and species concentrations across the mass transport zone adjacent the electrode surface (Fig. 1) and adsorbed intermediates, such as $\text{Fe}(\text{I})\text{-OH}$ species (Diaz et al., 2008), forming on the electrode surface before metal deposition. Evaluating the “equilibrium” fractionation between these intermediate species and plated metal would be a pointless exercise given that the formation of intermediate surface species is under the control of chemical kinetics. Instead it can be assumed for the purposes of this discussion that “equilibrium” fractionation is between the overall bulk composition of the aqueous metal species and the final metallic product. Isotope fractionation between species in chemical equilibrium (step 1) are predicted to be small (ranging from -0.9‰ to -3.0‰) and should have a temperature dependence opposite to what is observed here. Theoretical studies of aqueous Fe complexes (Schauble et al., 2001; Anbar et al., 2005) predict an equilibrium fractionation factor ranging from $\alpha^{56\text{Fe}} = 0.9991$ to 0.99875 ($\delta^{56}\text{Fe} \sim -0.9\text{‰}$ to -1.25‰) between metallic $\alpha\text{-Fe}$ and the aqueous Fe complex at 25 °C. This indicates that if the iron hexaaqua complex were the main species being reduced at the electrode surface, the equilibrium

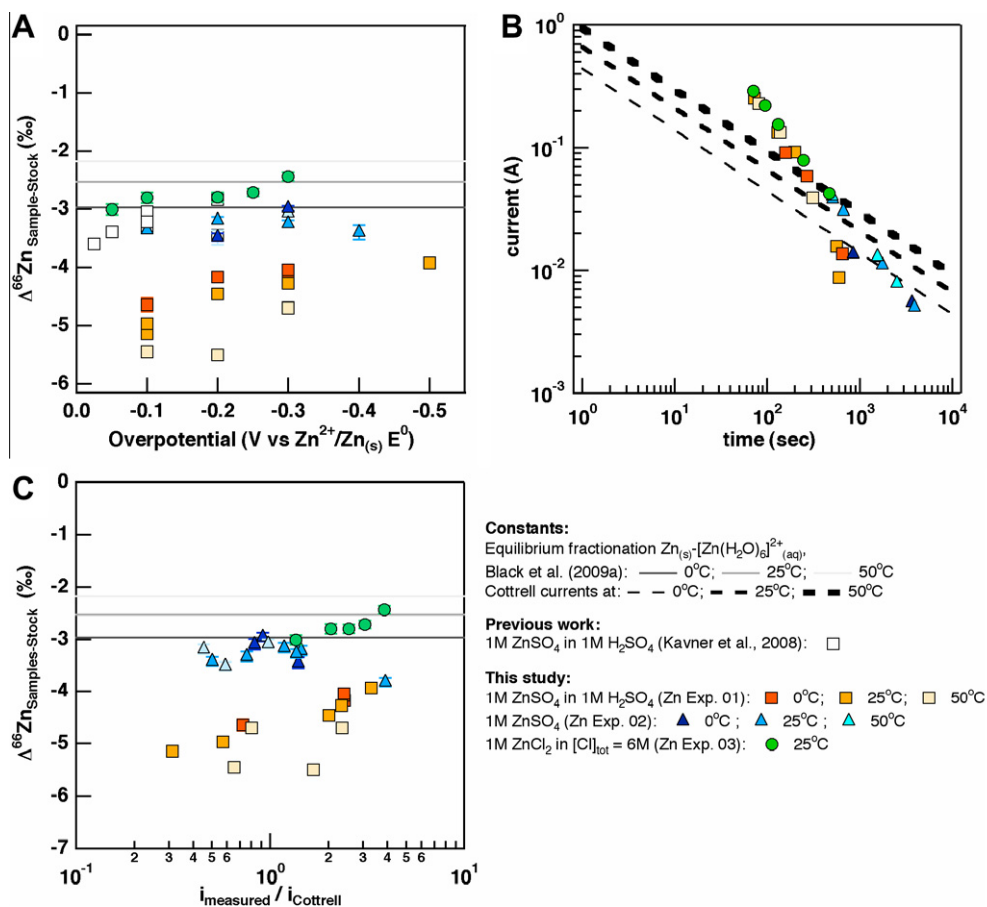


Fig. 5. Results from zinc experiments showing: (A) $\Delta^{66}Zn$ vs. overpotential; (B) effect of temperature on the diffusion-limiting Cottrell current calculated for 1.0 M stock solution of zinc (dashed lines) with experimental current superimposed; (C) $\Delta^{66}Zn$ vs. the ratio of experimental current to Cottrell diffusion-limiting current.

isotope fractionation would result in a metal deposit 0.9–1.25‰ lighter than the Fe in solution. Fig. 4A shows that this predicted fractionation ($\Delta^{56/54}Fe_{Equilibrium} = -0.9\text{‰}$ to -1.25‰ at 25 °C) is too small to explain the large fractionations seen in experiments run at low overpotentials ($\eta < -1.0$ V, Fig. 4A). Similarly, theoretical calculations (Black et al., 2009a) show that the equilibrium fractionation factor between metallic Zn and the aqueous $[Zn(H_2O)_6]^{2+}_{(aq)}$ complex ($\Delta^{66/64}Zn_{Equilibrium} = -2.5\text{‰}$ at 25 °C) is much smaller than the observed fractionations (Fig. 5A).

Stable isotope theory (Bigeleisen and Mayer, 1947; Urey, 1947; Schauble et al., 2001) also predicts that the fractionation should scale as a function of the inverse of temperature squared ($1/T^2$). This means that if the fractionation observed were due entirely to equilibrium fractionation between different Fe species, one would expect to see an increase in the observed fractionation with decreasing temperature (Hill and Schauble, 2008; Hill et al., 2009). In fact the opposite trend is seen in the case of Iron Exp. 01 (Fig. 4A) and Zinc Exp. 02 (Fig. 5A). The behavior on the three-isotope plots (Fig. 6) is further evidence that a process other than equilibrium isotope partitioning is taking place in these experiments. Therefore, although isotope fractionations associated with chemical speciation changes

may help to determine the fractionations, equilibrium processes are not the primary governing mechanisms that determine the overall fractionation. Therefore, our next step is to evaluate the effect of mass transport to the electrode on the observed isotope fractionations.

4.2. Mass transport and electrochemical kinetic effects

It is unlikely that diffusion alone is responsible for the observed fractionation. Isotope-dependent diffusion coefficients for Fe^{2+} and Zn^{2+} in chloride solutions at 20 °C has been measured to be $D_{54Fe} = 1.000085 \cdot D_{56Fe}$ and $D_{64Zn} = 1.000058 \cdot D_{66Zn}$ (Rodushkin et al., 2004). These values indicate that fractionation of the stable isotopes of iron and zinc due to diffusion is much smaller than we observe in these experiments. An upper bound to the fractionation due to diffusion can be calculated using the kinetic theory for the diffusion of two isotopologue species, m_1 and m_2 , through a gas of molecular weight, M : $D_1/D_2 = (m_2(m_1 + M)/m_1(m_2 + M))^{0.5}$ (Richter et al., 2003; Rodushkin et al., 2004). In this case, the calculated fractionation for unsolvated metal ions through water is equivalent to $\delta^{56}Fe = -2.25\text{‰}$ and $\delta^{66}Zn = -1.67\text{‰}$; and -0.30‰ and -0.27‰ , respectively, for hexaaquo species.

These fractionations are still smaller than our observed experimental fractionations.

The second hypothesis to consider is that mass transport processes coupled with electrochemical kinetics may be responsible for the fractionation trends seen in the Fe and Zn systems as a function of overpotential and temperature (Figs. 4 and 5). The isotope effects of mass transport-limited iron deposition at an electrode have been explicitly examined for the case of a planar electrode (Kavner et al., 2009) and a rotating disc electrode (Black et al. (2010)). In both cases, mass transport-limited kinetics strongly attenuates the observed fractionations. Diffusion to a planar electrode is described by Fick's second law (Bard and Faulkner, 2001), a solution to which under these conditions (Bard and Faulkner, 2001) leads to the definition of a diffusion-limiting or "Cottrell" current (i_d):

$$i_d(t) = \frac{nFA\sqrt{D_M}}{\sqrt{\pi t}} \quad (1)$$

where t is time, n is the stoichiometric number of electrons being transferred, F is Faradays constant, A is the surface area of the planar electrode, and D_M is the diffusion coefficient for metal (M). Diffusion is a thermally activated process, where diffusion coefficients scale in an Arrhenius relationship: $D = D_0 \exp(-E_A/RT)$. The diffusion coefficients for iron and zinc (Vanysek, 2010) can be extrapolated to the temperature of the experiments given estimates of the activation energies for diffusion (Zn: $E_A \sim 22.1$ kJ mol⁻¹ (Adhyapak, 1986); Fe: $E_A \sim 41$ kJ mol⁻¹ (Agarwal, 1962)). Diffusion to a planar electrode is described by Fick's second law (Bard and Faulkner, 2001). Using the extrapolated diffusion coefficients the effect of temperature on Cottrell diffusion-limiting current (Bard and Faulkner, 2001; Kavner et al., 2009) as a function of time can be calculated and compared to the average currents observed in experiments (Table 3 and Figs. 4B, 5B).

The observed currents span almost six orders of magnitude in the iron experiments (Fig. 4B) and three orders of magnitude in the zinc experiments (Fig. 5B). Superimposed Cottrell currents as a function of time (dashed lines, Figs. 4B and 5B) have a shallower slope than the experimental data and span a much wider current range as a function of temperature, with higher upper values for the diffusion-limiting current at higher temperatures. This suggests that mass transport limitations and the $\Delta^X M_{\text{MassTransport}}$ term is less important at higher temperatures as diffusion to the electrode surface increases and may partly explain the increase in fractionation if a larger $\Delta^X M_{\text{Electrochemical}}$ term predominates with increasing temperature.

To further assess the role of mass transport, isotope fractionation is plotted as a function of the ratio of the plating current to the Cottrell limiting current (Figs. 4C and 5C) (Kavner et al., 2009), in a similar manner to a study by Watson and Müller (2009) where the effect of the ratio of crystal growth rate to diffusivity in the growth medium is used in isotopic models of crystal growth. This ratio is a qualitative assessment of the mass transport regime in the experiments (illustrated in Fig. 1A and B). A clear trend emerges in the majority of data sets where fractionation increases as the current ratio decreases and charge-transfer

kinetics are limiting the rate of metal deposition. At higher current ratios, where mass transport kinetics and diffusion to the electrode surface are limiting the rate of metal deposition, much smaller fractionations are observed.

This analysis appears to reconcile the current planar electrode data with the earlier data (Kavner et al., 2005, 2008). For iron, a comparison of the Kavner et al. (2005) data with the current FeCl₂ data shows a u-shaped fractionation as a function of current (Fig. 4C). At low deposition rates (low currents), low fractionations are observed. As deposition rate increases, the fractionation increases. As the deposition rate increases further, mass transport to the electrode becomes more limiting, and fractionation decreases again. The bottom of this u-shaped curve occurs close to the point where the reaction kinetics are approximately equal to mass transport kinetics ($i_{\text{measured}}/i_{\text{Cottrell}} \sim 1$). However, for the iron sulfate solution, much larger fractionations are observed at lower deposition rates. This may be due to speciation-related isotope differences between the Fe-SO₄ complexes and the Fe-Cl₂ complexes. A similar analysis could not be used to compare the Kavner et al. (2008), zinc measurements with the current measurements, because reaction efficiencies were not measured in those experiments. However, the extent of fractionation observed in metallic zinc plated from Zn-Cl₂ stocks in this study, show similar fractionation values and trends with overpotential.

By examining isotope fractionation as a function of experimental current relative to mass transport limiting current, the temperature effect can be re-assessed. Because mass transport is strongly thermally activated, the higher temperature experiments have smaller $i_{\text{measured}}/i_{\text{Cottrell}}$ ratios than lower temperature experiments performed at the same overpotential. Therefore, it appears that the observation of increasing isotope fractionation with temperature can be explained by a thermal enhancing of the rates of mass transport of reactant to the electrode surface. The original theory developed by Kavner et al. (2005) appears to be most relevant when applied to their iron data set, where mass transport limitations may be minimal due to low rates of electrochemical deposition. However, more detailed reservoir models are needed to separate the effects of mass transport from electron transfer kinetics and the subsequent effect on isotopic fractionation in the in final products.

5. CONCLUSIONS

Separating stable isotopes of transition metals is usually difficult, and tends to result in small fractionations. Here, we use electroplating to generate very large isotope fractionations during a redox process. The fractionations observed in our laboratory are as large as the variability observed in natural systems. Although the experiments performed here—electrodeposition of metals from M(II) aqueous species—are not the identical to the processes that occur in natural systems (e.g., usually Fe(II)/Fe(III)), the concepts and the underlying theory are equally relevant. The Marcus-Kavner theory (Kavner et al., 2005) predicts an isotopic fractionation will occur during any electrochemical charge-transfer process. Mass transport is relevant for all reaction kinetics, as is consideration of

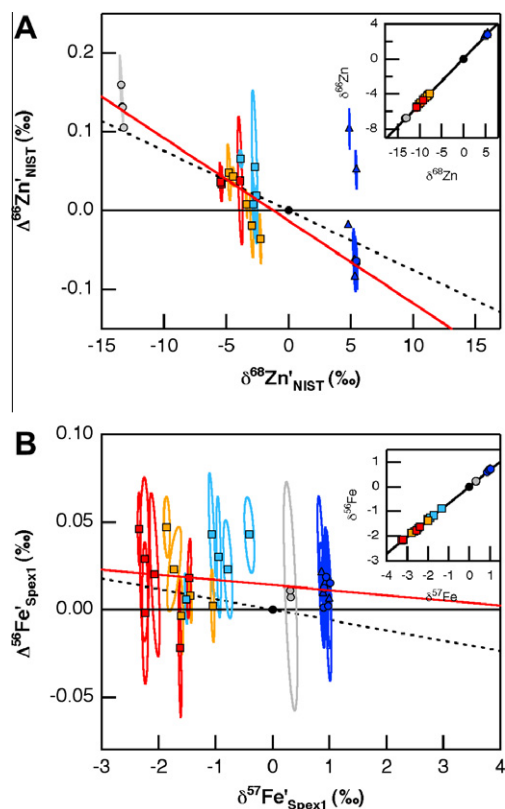


Fig. 6. Three-isotope plots of (A) $\Delta^{66}\text{Zn}'_{\text{NIST}}$ vs. $\delta^{68}\text{Zn}'_{\text{NIST}}$ with $\delta^{66}\text{Zn}$ vs. $\delta^{68}\text{Zn}$ inset, Zinc Experiment 01; (B) $\Delta^{56}\text{Fe}'_{\text{Spex1}}$ vs. $\delta^{57}\text{Fe}'_{\text{Spex1}}$ with $\delta^{56}\text{Fe}$ vs. $\delta^{57}\text{Fe}$ inset, Iron Experiment 01. Equilibrium mass-dependent fractionation line (solid, 0 on y axis); kinetic mass-dependent fractionation line (dashed) using atomic masses (Young and Galy, 2004). Weighted best fit to data (red solid line). (For interpretation of the references to color in this figure legend, the reader is referred to the web version of this article.)

isotope fractionations due to speciation changes. Although the details of extent of fractionations may vary from process to process (and indeed—we observe this as we change solution chemistry in our systems) the underlying principles apply to all of these systems.

Fig. 1 represents a simplification of a dynamic interplay between the processes controlling deposition of metal at a charged interface. The results presented here suggest the overall fractionation measured in metal samples is a result of contributions from all three processes in Fig. 1. Differences in aqueous speciation result in differences in the magnitude of fractionation, but predicted equilibrium isotope effects ($\Delta^{56}\text{Fe}_{\text{Fe(s)}-\text{[Fe(H}_2\text{O)}_6]^{2+}}^{25^\circ\text{C}} = -0.9\text{‰}$ (Schauble et al., 2001); $\Delta^{66}\text{Zn}_{\text{Zn(s)}-\text{[Zn(H}_2\text{O)}_6]^{2+}}^{25^\circ\text{C}} = -2.5\text{‰}$ (Black et al., 2009a)) are small in comparison to the overall fractionations observed (at 25 °C: $\Delta^{56}\text{Fe}$ up to -3.82‰ ; $\Delta^{66}\text{Zn}$ up to -5.14‰) and predict the opposite trends with changing temperature in some cases. The overpotentials applied in these experiments were quite large and led to mass transport limitations. All the data fall out along a clear trend when examining the mass transport regime, with larger fractionations observed at small deposition currents, where charge-transfer kinetics are limiting and fractionation is

systematically attenuated by a smaller diffusion-driven fractionation at higher deposition currents where mass transport limitations dominate.

Together, these data bolster the hypothesis of a large isotope fractionation due to the electron transfer step at the electrode. The temperature effect explored here in mass transport limiting regimes, where fractionation is increasing with increasing temperature, is counterintuitive to stable isotope theory where fractionation is expected to decrease with increasing temperature. These temperature trends can be explained when examining the experimental reaction currents (deposition rates) against a mass transport limiting current (calculated Cottrell current) where this ratio decreases with increasing temperature, or in other words mass transport to the electrode is thermally activated and increases as temperature increases. An examination of the temperature effect upon fractionation in a non-mass transport limiting regime is needed for a more complete understanding of the electrochemical isotope effect predicted by Marcus–Kavner theory. Studies are currently underway to examine this effect using rotating disc electrodes where the mass transport regime can be directly controlled.

The processes reported here may be valuable for interpreting isotope signals in the natural environment. For example, we find that in mass transport-limited reactions there is a positive correlation between the magnitude of isotope fractionation and temperature, and a negative correlation between the magnitude of isotope fractionation and reaction driving force. In the absence of mass transport limitation theory predicts the opposite relationships, with isotope effects decreasing at higher temperatures and increasing with higher reaction driving force. Correlations between the magnitude of isotope fractionation and temperature or driving force may therefore be used as a tool to determine whether a natural system is mass transport limited. This research also helps to establish the magnitude of different isotope effects. While the large isotope effects associated with electroplating are unlikely to be seen in natural systems, the diffusion isotope effect for M(II) species may be applicable to natural and environmental samples. For example, this work demonstrates that the diffusion isotope effect for Fe in 0.8 M FeCl_2 is less than 1‰ and that diffusion isotope effects for Zn in 1 M ZnSO_4 or 1 M ZnCl_2 is less than 2.5‰. In future experiments, electroplating could provide a new tool for measuring the exact magnitude of these diffusion isotope effects. Mass transport limitation and diffusion are common natural processes that affect the fractionation of metal isotopes. By studying these processes in controlled laboratory experiments, we can better understand how these signals will be recorded in the natural environment.

ACKNOWLEDGMENTS

We thank Professor Edwin Schauble for his input and discussion of equilibrium isotope effects, Professor Jess Adkins for access to facilities at Caltech and Drs. Eric Tonui and Dr. Karen Zeigler for technical support. This work was funded by NASA Exobiology NNG05GQ92G (A.K.).

REFERENCES

- Adhyapak N. G. (1986) Activation energy of self-diffusion of zinc, chloride and chromate ions. *J. Radioanal. Nucl. Chem.* **103**, 379–385.
- Agarwal H. P. (1962) Variation of the diffusion coefficient of ferric ion (0.002 M in N sulfuric acid) with temperature and calculation therefrom of the energy and entropy of activation. *J. Electroanal. Chem.* **A56**, 108–114.
- Anbar A. D. (2004) Iron stable isotopes: beyond biosignatures. *Earth Planet. Sci. Lett.* **217**, 223–236.
- Anbar A. D., Jarzecki A. A. and Spiro T. G. (2005) Theoretical investigation of iron isotope fractionation between $\text{Fe}(\text{H}_2\text{O})_6^{3+}$ and $\text{Fe}(\text{H}_2\text{O})_6^{2+}$: implications for iron stable isotope geochemistry. *Geochim. Cosmochim. Acta* **69**, 825–837.
- Bard A. J. and Faulkner L. R. (2001) *Electrochemical Methods: Fundamentals and Applications*. John Wiley & Sons, Inc., USA.
- Beard B. L., Johnson C. M., Cox L., Sun H., Nealon K. H. and Aguilar C. (1999) Iron isotope biosignatures. *Science (Washington, DC)* **285**, 1889–1892.
- Bigeleisen J. and Mayer M. G. (1947) Calculation of equilibrium constants for isotopic exchange reactions. *J. Chem. Phys.* **15**, 261–267.
- Black J. R., John S., Schauble Edwin A. and Kavner A. (2009a) Resolving equilibrium and kinetic Zn isotope fractionations. *Geochim. Cosmochim. Acta* **73**, A127.
- Black J. R., Umeda G., Dunn B., McDonough W. F. and Kavner A. (2009b) The electrochemical isotope effect and lithium isotope separation. *J. Am. Chem. Soc.* **131**, 9904–9905.
- Black J. R., Young E. and Kavner A. (2010) Electrochemically controlled iron isotope fractionation. *Geochim. Cosmochim. Acta* **74**, 809–817.
- Diaz S. L., Calderon J. A., Barcia O. E. and Mattos O. R. (2008) Electrodeposition of iron in sulphate solutions. *Electrochim. Acta* **53**, 7426–7435.
- Ellis A. S., Johnson T. M. and Bullen T. D. (2002) Fate of hexavalent chromium in the environment. *Science (Washington, DC, USA)* **295**, 2060–2062.
- Epelboin I., Ksouri M. and Wiart R. (1975) Interpretation of the spatial structure of electrolytic zinc deposits by a surface diffusion-interfacial reactions coupling. *J. Electroanal. Chem. Interfacial Electrochem.* **58**, 433–437.
- Grujicic D. and Pesic B. (2005) Iron nucleation mechanisms on vitreous carbon during electrodeposition from sulfate and chloride solutions. *Electrochim. Acta* **50**, 4405–4418.
- Heinrich C. A. and Seward T. M. (1990) A spectrophotometric study of aqueous iron (II) chloride complexing from 25 to 200 °C. *Geochim. Cosmochim. Acta* **54**, 2207–2221.
- Hill P. S. and Schauble E. A. (2008) Modeling the effects of bond environment on equilibrium iron isotope fractionation in ferric aquo-chloro complexes. *Geochim. Cosmochim. Acta* **72**, 1939–1958.
- Hill P. S., Schauble E. A., Shahar A., Tonui E. and Young E. D. (2009) Experimental studies of equilibrium iron isotope fractionation in ferric aquo-chloro complexes. *Geochim. Cosmochim. Acta* **73**, 2366–2381.
- John S. G., Park J. G., Zhang Z. and Boyle E. A. (2007) The isotopic composition of some common forms of anthropogenic zinc. *Chem. Geol.* **245**, 61–69.
- Johnson C. M., Beard B. L. and Roden E. E. (2008) The iron isotope fingerprints of redox and biogeochemical cycling in modern and ancient earth. *Annu. Rev. Earth Planet. Sci.* **36**, 457–493.
- Johnson C. M., Skulan J. L., Beard B. L., Sun H., Nealon K. H. and Braterman P. S. (2002) Isotopic fractionation between Fe(III) and Fe(II) in aqueous solutions. *Earth Planet. Sci. Lett.* **195**, 141–153.
- Kavner A., Bonet F., Shahar A., Simon J. and Young E. (2005) The isotopic effects of electron transfer: an explanation for Fe isotope fractionation in nature. *Geochim. Cosmochim. Acta* **69**, 2971–2979.
- Kavner A., John S. G., Sass S. and Boyle E. A. (2008) Redox-driven stable isotope fractionation in transition metals: application to Zn electroplating. *Geochim. Cosmochim. Acta* **72**, 1731–1741.
- Kavner A., Shahar A., Black J. R. and Young E. (2009) Iron isotopes at an electrode: diffusion-limited fractionation. *Chem. Geol.* **267**, 131–138.
- Liu W., Etschmann B., Foran G., Shelley M. and Brugger J. (2007) Deriving formation constants for aqueous metal complexes from XANES spectra: Zn^{2+} and Fe^{2+} chloride complexes in hypersaline solutions. *Am. Mineral.* **92**, 761–770.
- Marcus R. A. (1964) Generalization of the activated complex theory of reaction rates: I. Quantum mechanical treatment. *J. Chem. Phys.* **41**, 2614–2623.
- Marcus R. A. (1965) Theory of electron-transfer reactions: VI. Unified treatment for homogeneous and electrode reactions. *J. Chem. Phys.* **43**, 679–701.
- Ninkovic R., Miladinovic J., Todorovic M., Grujic S. and Rard J. A. (2007) Osmotic and activity coefficients of the $\{x\text{ZnCl}_2 + (1-x)\text{ZnSO}_4\}(\text{aq})$ system at 298.15 K. *J. Solut. Chem.* **36**, 405–435.
- Nordstrom D. K. (1977) Thermochemical redox equilibria of ZoBell's solution. *Geochim. Cosmochim. Acta* **41**, 1835–1841.
- Parkhurst D. L. (1995) *User's guide to PHREEQC: a computer program for speciation, reaction-path, advective-transport, and inverse geochemical calculations*. Water Resources Division, Geological Survey, Lakewood, CO, USA.
- Rademacher L. K., Lundstrom C. C., Johnson T. M., Sanford R. A., Zhao J. and Zhang Z. (2006) Experimentally determined uranium isotope fractionation during reduction of hexavalent U by bacteria and zero valent iron. *Environ. Sci. Technol.* **40**, 6943–6948.
- Richter F. M., Davis A. M., DePaolo D. J. and Watson E. B. (2003) Isotope fractionation by chemical diffusion between molten basalt and rhyolite. *Geochim. Cosmochim. Acta* **67**, 3905–3923.
- Rodushkin I., Stenberg A., Andren H., Malinovsky D. and Baxter D. C. (2004) Isotopic fractionation during diffusion of transition metal ions in solution. *Anal. Chem.* **76**, 2148–2151.
- Rouxel O. J., Bekker A. and Edwards K. J. (2005) Iron isotope constraints on the Archean and Paleoproterozoic ocean redox state. *Science (Washington, DC, USA)* **307**, 1088–1091.
- Rudolph W. W., Brooker M. H. and Tremaine P. (1999) Raman- and infrared spectroscopic investigation of aqueous ZnSO_4 solutions from 8 deg to 165 deg. Inner- and outer-sphere complexes. *Z. Phys. Chem. (Muenchen)* **209**, 181–207.
- Schauble E. A., Rossman G. R. and Taylor H. P. (2001) Theoretical estimates of equilibrium Fe-isotope fractionations from vibrational spectroscopy. *Geochim. Cosmochim. Acta* **65**, 2487–2497.
- Teng F.-Z., Dauphas N. and Helz R. T. (2008) Iron isotope fractionation during magmatic differentiation in Kilauea Iki lava lake. *Science (Washington, DC, USA)* **320**, 1620–1622.
- Urey H. C. (1947) Thermodynamic properties of isotopic substances. *J. Chem. Soc.* **1947**, 562–581.
- Vanysek P. (2010) "Ionic conductivity and diffusion at infinite dilution". In *CRC Handbook of Chemistry and Physics*, 90th Edition, Internet Version 2010, (ed. David R. Lide), CRC Press/Taylor and Francis, Boca Raton, FL.

- Wagman D. D., Evans W. H., Parker V. B., Schumm R. H., Halow I., Bailey S. M., Churney K. L. and Nuttall R. L. (1982) *J. Phys. Chem. Ref. Data*, **11** (Suppl. 2). *The NBS Tables of Chemical Thermodynamic Properties. Selected Values for Inorganic and C1 and C2 Organic Substances in SI Units*.
- Watson E. B. and Müller T. (2009) Non-equilibrium isotopic and elemental fractionation during diffusion-controlled crystal growth under static and dynamic conditions. *Chem. Geol.* **267**, 111–124.
- Welch S. A., Beard B. L., Johnson C. M. and Braterman P. S. (2003) Kinetic and equilibrium Fe isotope fractionation between aqueous Fe(II) and Fe(III). *Geochim. Cosmochim. Acta* **67**, 4231–4250.
- Weyer S. (2008) What drives iron isotope fractionation in magma? *Science (Washington, DC, USA)* **320**, 1600–1601.
- Williams H. M., McCammon C. A., Peslier A. H., Halliday A. N., Teutsch N., Levasseur S. and Burg J.-P. (2004) Iron isotope fractionation and the oxygen fugacity of the mantle. *Science (Washington, DC, USA)* **304**, 1656–1659.
- Young E. D. and Galy A. (2004) The isotope geochemistry and cosmochemistry of magnesium. *Rev. Mineral. Geochem.* **55**, 197–230.
- Young E. D., Galy A. and Nagahara H. (2002) Kinetic and equilibrium mass-dependent isotope fractionation laws in nature and their geochemical and cosmochemical significance. *Geochim. Cosmochim. Acta* **66**, 1095–1104.
- ZoBell C. E. (1946) Oxidation–reduction potential of marine sediments. *Am. Assoc. Pet. Geol. Bull.* **30**, 477–513.

Associate editor: James Farquhar